Applied Catalysis B: Environmental 163 (2015) 370–381

Contents lists available at ScienceDirect

Applied Catalysis B: Environmental

journal homepage: www.elsevier.com/locate/apcatb

Acid catalytic properties of reduced tungsten and niobium-tungsten oxides

Chaochao Yue[a], Xiaochun Zhu[a], Marcello Rigutto[b,1], Emiel Hensen[a,*]

[a] Inorganic Materials Chemistry, Eindhoven University of Technology, P.O. Box 513, 5600 MB Eindhoven, The Netherlands
[b] Shell Global Solutions International B.V., P.O. Box 38000, 1030 BN Amsterdam, The Netherlands

ARTICLE INFO

Article history:
Received 5 June 2014
Received in revised form 28 July 2014
Accepted 2 August 2014
Available online 15 August 2014

Keywords:
Tungsten oxide
Acidity
Reduction
Ammonia
Hydroisomerization

ABSTRACT

Tungsten oxide and mixed niobium–tungsten oxides were prepared by calcination of re-precipitated tungsten and niobium precursors. These materials were characterized by N_2 physisorption, XRD, XPS, UV–vis and UV Raman spectroscopy and H_2-TPR. With increasing calcination temperature the oxides were seen to transform from a mixture of h-WO_3 and HATB ($T<400\,^{\circ}C$) to predominantly h-WO_3 ($400\,^{\circ}C<T<470\,^{\circ}C$) and m-$WO_3$ ($T>470\,^{\circ}C$). Ammonium ion and ammonia are essential to retain the hexagonal structure of the intermediate phase. The reducibility of the various samples was linked to their structure. In-situ XRD point to formation of β-W in the presence of Pd when the precursor was deeply reduced. When the precursor predominantly contained h-WO_3, $(NH_4)_{0.33-x}(H_3O)_yWO_{3-z}$ was obtained upon reduction of tungsten and mixed niobium–tungsten oxide materials. These exhibited good performance in the bifunctional hydroisomerization of *n*-alkanes, outperforming amorphous silica–alumina and tungstated zirconia catalysts.

1. Introduction

Acid-catalyzed hydrocarbon conversion processes are pivotal in modern oil refineries. For isomerization and alkylation purposes, acidic chlorinated aluminas as well as strong mineral acids such as $AlCl_3$, H_2SO_4, HF are employed. The use of these acids poses significant corrosion and environmental problems. Therefore, zeolites and amorphous silica–aluminas have been developed as heterogeneous acid catalysts, for instance for (hydro)cracking of heavy oil fractions. There continues to be interest in the development of new solid acid materials [1–3]. Tungsten-oxides comprise a class of solid acids, which have been investigated in detail in the last two decades [4–11]. Bulk WO_3 has low surface area with no apparent strong Brønsted acidity. It is generally assumed that the Brønsted acidity is associated with partial reduction of the WO_x surface. Protons compensate the delocalized charge induced by partial reduction of W^{6+} centers. The pseudo-metallic W_3O phase formed by high-temperature reduction of WO_3 has been argued to provide high and stable hydroisomerization selectivity in hexane reforming [12]. The addition of metals like Pt and Pd typically increases acidity in the presence of hydrogen [13,14]. Arata and co-workers reported on bulk mixed tungsten–niobium oxides containing strong Brønsted acid sites, which were argued to derive from substitution of W^{6+} with Nb^{5+} in the surface of WO_3 [15]. It has been mentioned that such mixed oxides display similar acid strength as layered $HNbWO_6$ and the catalytic performance in cumene cracking of these materials is higher than aluminosilicates [15,16]. Arata's group also reported about WO_x supported on ZrO_2 (WO_x/ZrO_2) [4,5]. Several structural models for the acid sites in tungstated zirconia have been discussed [6,17–21]. It is known that tungsten oxide supported on $ZrO_x(OH)_{4-2x}$ is more acidic than when supported on well-defined ZrO_2 crystallites [19]. Kiely and co-workers investigated the nanoscale structures present in supported WO_3/ZrO_2 and proposed that subnanometer WO_x incorporating some zirconium cations hold the acid sites with capable of catalyzing methanol dehydration [9]. For reduced tungstated zirconia, it has been proposed that Brønsted acid sites form in WO_3 clusters of intermediate size on zirconia [18]. Combined with Pt, these supported tungsten oxides are active and selective catalysts for the hydroisomerization of *n*-alkanes [22–24].

The studies of the groups of Arata and Domen on tungsten-oxide based catalysts led us to study the structure, activation by calcination and reduction as well as the catalytic properties of bulk WO_3 samples. Bulk WO_3 was prepared by precipitation of an aqueous solution of ammonium metatungstate followed by calcination at different temperatures. A set of binary Nb–W oxides was prepared

* Corresponding author. Tel.: +31 40 2475178.
E-mail addresses: marcello.rigutto@shell.com (M. Rigutto), E.J.M.Hensen@tue.nl (E. Hensen).
[1] Tel.: +31 20 6303221; fax: +31 20 6303110.

http://dx.doi.org/10.1016/j.apcatb.2014.08.008
0926-3373/

in a similar manner a precursor containing Nb. XRD, UV–vis and Raman spectroscopy were used to follow the structural changes as a function of the calcination temperature. The reduction of these (mixed) oxides and their Pd-containing catalyst precursors were studied by TPR and XPS. The catalytic performance of the reduced samples was evaluated in the hydroisomerization of *n*-heptane and compared to zeolite, amorphous silica–alumina and WO_x/ZrO_2 reference catalysts.

2. Experimental methods

2.1. Preparation

An amount of 10 g of ammonium metatungstate hydrate (Sigma-Aldrich, 99.0%) was dissolved in 20 g water and stirred for 10 min at 70 °C. After slow evaporation of water at 70 °C, the powder was dried in an oven at 110 °C for 10 h. The dried powder was divided into several portions. Each portion was calcined in the air for 2 h at different temperatures, namely 380, 420, 450, 470 or 500 °C. The calcined samples were named WO_3-*T* with *T* denoting the calcination temperature. For comparison, mixed Nb-W oxides were also prepared at varying W/Nb ratios. For this purpose, solutions containing ammonium metatungstate hydrate and ammonium niobate oxalate hydrate in appropriate ratios were prepared and subjected to the slow evaporation procedure outlined above for the WO_3 precursor powder. The employed W/Nb ratios were between 5 and 120. The resulting powders were divided in two portions, one being calcined at 420 °C and the other at 450 °C for 2 h. These samples are denoted as NbW_x-420 and NbW_x-450 with *x* denoting W/Nb ratio.

To prepare Pd/WO_3 and Pd/NbW_x, an amount of 1.5 g of WO_3 or NbW_x powder was impregnated with 15 g of a solution of tetraamminepalladium nitrate (Sigma-Aldrich, 10 wt% in water) to reach a final Pd loading of 1.0 wt%. The excess solvent was evaporated and the final material was calcined at 300 °C for 2 h in air. These catalysts are denoted as Pd/WO_3-*T* (Pd/NbW_x-*T*).

Zirconia-supported WO_3 was prepared as described previously [14]. $ZrO_x(OH)_{4-2x}$ supports was first prepared by hydrolysis of 0.5 M $ZrOCl_2$ (Aldrich Chemicals, >98%) aqueous solutions fed at 500 $cm^3\ h^{-1}$ into a well-stirred vessel with a pH of 10 held constant by the controlled addition of 14 M NH_4OH. The precipitate was dried at 150 °C overnight after residual Cl^- ions were removed (<10 ppm) by thorough washing. The dried $ZrO_x(OH)_{4-2x}$ solids were impregnated to the point of incipient wetness with aqueous solutions of ammonium metatungstate of appropriate concentration. These samples were placed in shallow quartz boats, heated to the final oxidation temperature of 800 °C, and held isothermal for 3 h in dry air. Tungsten oxide loadings are reported as the weight percentage of WO_3 (4.5, 13.5 and 18 wt% WO_3) in the calcined samples. Samples are denoted as WZr(*x*) with *x* being the WO_3 loading. Pd loading was done in the same way as for the unsupported WO_3-*T* samples.

2.2. Characterization

Powder X-ray diffraction (XRD) patterns were measured on a Bruker D4 Endeavor using Cu Kα radiation. Nitrogen sorption was measured on a Micromeritics Tristar 3000 system in static measurement mode. The samples were outgassed at 120 °C for 3 h prior to the sorption measurements. The Brunauer–Emmett–Teller (BET) equation was used to calculate the specific area from the adsorption data (p/p_0 = 0.05–0.25). Scanning electron microscopy (SEM) was performed using a Philips environmental scanning electron microscope FEIXL-30 ESEM FEG in high-vacuum mode at low voltage. TG profiles were measured on Mettler Toledo TGA/DSC STAR system using an O_2 flow of 40 mL/min and a protective N_2 flow of 20 mL/min. The powder was in an open alumina crucible and heated at a rate of 10 °C/min. UV Raman spectra was recorded with a Jobin–Yvon triple stage spectrometer with a spectral resolution of 2 cm^{-1}. The laser line at 325 nm of a Lexel 95-SHG laser was used as excitation source at an output of 10 mW. The power of the laser on the sample was about 2 mW. UV–vis spectra were recorded on a Shimadzu UV-2401 PC spectrometer in diffuse-reflectance mode using an integrating sphere (internal diameter 60 mm) and $BaSO_4$ was used as the reference. Temperature-programed reduction (TPR) experiments were carried out in a flow apparatus equipped with a fixed-bed reactor, a computer-controlled oven and a thermal conductivity detector. Prior to TPR, the catalyst was treated by a flowing mixture of 4 vol% O_2 in He at 30 °C. Then the sample was reduced in 4 vol% H_2 in N_2 at a flow rate of 8 ml/min, while heating from room temperature to 800 °C at a ramp rate of 10 °C/min and keeping for 60 min at 800 °C. The H_2 signal was calibrated using a CuO/SiO_2 reference catalyst.

X-ray Photoelectron Spectroscopy (XPS) was done on a Kratos AXIS Ultra spectrometer, equipped with a monochromatic Al Kα X-ray source and a delay-line detector (DLD). Spectra were obtained using an aluminum anode (Al Kα = 1486.6 eV) operating at 150 W, with survey scans at constant pass energy of 160 eV and region scans at a constant pass energy of 40 eV. The background pressure was 2×10^{-9} mbar. XP spectra were fitted with the CASA-XPS software. Quasi-in situ XPS measurements were performed after reduction of the samples in a tubular stainless reactor. The samples were heated at a rate of 10 °C/min from room temperature to 440 °C in a flow of H_2 at 35 bar. After cooling to room temperature, closing valves at the in- and outlet of the reactor prevented interaction with air. The samples for XPS measurements were then prepared in an Ar-flushed glove box.

2.3. Catalytic activity measurements

The acidity of the WO_3-based samples was evaluated from catalytic activity measurements in the hydroconversion of *n*-heptane. For this purpose, the oxides were first loaded with Pd. The resulting materials were calcined at 300 °C. Prior to testing, the catalysts were reduced at 440 °C at 35 bar in flowing hydrogen. Hydroconversion of *n*-heptane was carried out at 35 bar at a H_2/hydrocarbon ratio of 24 mol/mol. The reaction temperature was lowered from 440 °C till 200 °C at a rate of 0.2 °C/min. The conversion of *n*-heptane involves its dehydrogenation catalyzed by the noble metal, isomerization or β-scission by strong Brønsted acid sites and hydrogenation of the *i*-olefins to *i*-paraffins. The activity of the catalyst is expressed as the temperature at which a hydrocarbon conversion of 40% was achieved. From the temperature required to obtain 40% conversion, relative values for the rate constant *k* for two catalysts at a reference temperature T_{ref} can be determined using the expression

$$\ln(k_1/k_2) = E_{act,1}/R_g(1/T_{40,1} - 1/T_{ref}) - E_{act,2}/R_g(1/T_{40,2} - 1/T_{ref}) \quad (1)$$

or, if we choose the second catalyst as the reference $T_{ref} = T_{40,2}$

$$\ln(k/k_{ref}) = E_{act}/R_g(1/T_{40} - 1/T_{40,ref}) \quad (2)$$

in which E_{act} is the activation energy (J/mol) and R_g the gas constant (J/mol K). Here we choose Pd/WO_3-380 as the reference catalyst.

3. Results and discussion

Solid tungsten oxide powders were prepared by dissolving ammonium metatungstate (AMT), $(NH_4)_6[H_2W_{12}O_{40}]\cdot 4H_2O$, followed by slow evaporation of water, precipitation and calcination at temperatures in the 380–500 °C range. The XRD patterns of the

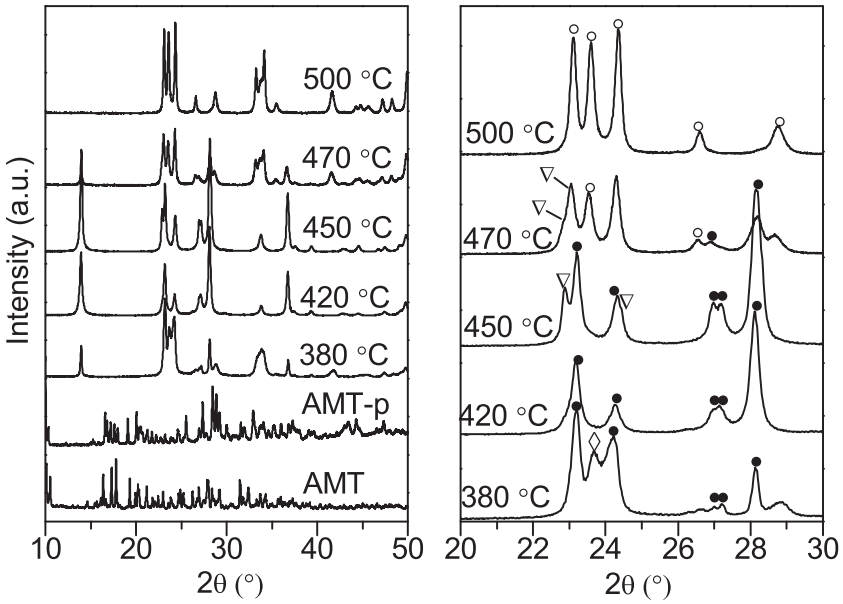

Fig. 1. XRD patterns of WO_3 prepared by precipitation and calcined at increasing temperatures (AMT: ammonium metatungstate hydrate, precursor material obtained by evaporating water from an AMT solution at 70 °C, (○) m-WO_3, (●) h-WO_3, (◊) HATB and (▽) H_xWO_{3-y} (THTB) (the right panel shows a magnified region of the left spectra).

Table 1
Physico-chemical properties of WO_3 and NbW_x materials.

Sample	S.A.[a] (m^2/g)	W/Nb [b]	XRD			TGA			Band gap (eV)
			h-WO_3 (%)	HATB (%)	m-WO_3 (%)	THTB (%)	H_2O_{phs} [c] (%)	$(H_2O+NH_3)_{struct.}$ [d] (%)	
WO_3-380	12	–	57	54	0	0	0	0.5	3.09
WO_3-420	4	–	93	7	0	0	1.0	0.5	3.12
NbW_{10}-420	21	12	100	0	0	0	1.1	0.7	3.20
NbW_{15}-420	6	25	100	0	0	0	1.0	0.7	3.15
NbW_{30}-420	6	45	100	0	0	0	0.6	0.9	2.99
NbW_{45}-420	8	72	100	0	0	0	0.8	0.7	3.16
NbW_{120}-420	12	220	100	0	0	0	0.8	0.7	3.27
WO_3-450	7	–	79	0	0	21	0.8	0.1	3.09
NbW_{10}-450	18	12	84	0	4	12	0.3	0.2	3.01
NbW_{15}-450	6	23	82	0	0	18	0.5	0.2	2.96
NbW_{30}-450	7	40	89	0	3	8	0.4	0.3	3.01
NbW_{45}-450	5	65	86	0	5	9	0.5	0.2	2.95
NbW_{120}-450	11	220	56	0	40	4	0.4	0.1	3.00
WO_3-470	7	–	34	0	66	0	0.4	0	2.99
WO_3-500	6	–	4	0	96	0	0.2	0	2.89
AMT	–	–	–	–	–	–	–	–	3.46
WO_3	3	–	–	–	–	–	–	–	2.76

[a] Surface area.
[b] Ratio of W to Nb calculated by XPS.
[c] Physisorbed water.
[d] Structural water and ammonia.

resulting powders including the starting AMT and the reprecipitated powder from the aqueous AMT solution are shown in Fig. 1 and Table 1. The structure of the powder obtained after drying is different from AMT due to the loss of crystal water [25–27]. When the starting material was calcined at 380 °C, the material contains hexagonal tungsten bronze (HATB), $(NH_4)_{0.33-x}WO_{3-z}$ with the peak at 23.67° and hexagonal tungsten oxide (h-WO_3) with the peaks at 23.19 and 24.23° [11]. The difference between HATB and h-WO_3 is the lower occupancy with ammonium ions and ammonia of the six-membered ring channels of the structure of h-WO_3 [11]. The presence of reduced W cations also contributes to the small differences in the XRD patterns of h-WO_3 and HATB [28]. Increasing the calcination temperature results in pronounced changes. The XRD pattern of WO_3-420 shows that there is no HATB phase anymore and the material is nearly pure h-WO_3 (viz. the two peaks at 23.17 and 24.24°). The shoulder at 22.87° points to the presence of a small amount of tetragonal hydrogen tungsten bronze (THTB), H_xWO_{3-z}. After calcination at 450 °C, this reflection is more intense indicating that the removal of ammonia from h-WO_3 and structural rearrangements result in formation of more THTB. Calcination at 470 °C transforms the powder into m-WO_3 with residual amounts of h-WO_3 and THTB. Finally, the pattern of the material obtained by air calcination at 500 °C is almost exclusively due to m-WO_3.

The evolution of the XRD patterns bears resemblance with the trends observed in the thermal decomposition of ammonium metatungstate [27] and ammonium paratungstate ($(NH_4)_{10}[H_2W_{12}O_{42}]\cdot 4H_2O$) [29]. Ammonium paratungstate (APT) transforms into ammonium metatungstate (AMT) at intermediate temperatures [26]. The most salient points of these studies from literature are that (i) an amorphous phase is formed from the precursor by release of NH_3 and H_2O from the tungstate precursor up to 370 °C, (ii) this amorphous phase transforms into HATB or h-WO_3 in the temperature range 370–450 °C and (iii) the intermediate phases are oxidized to m-WO_3 at temperatures above 500 °C. Based

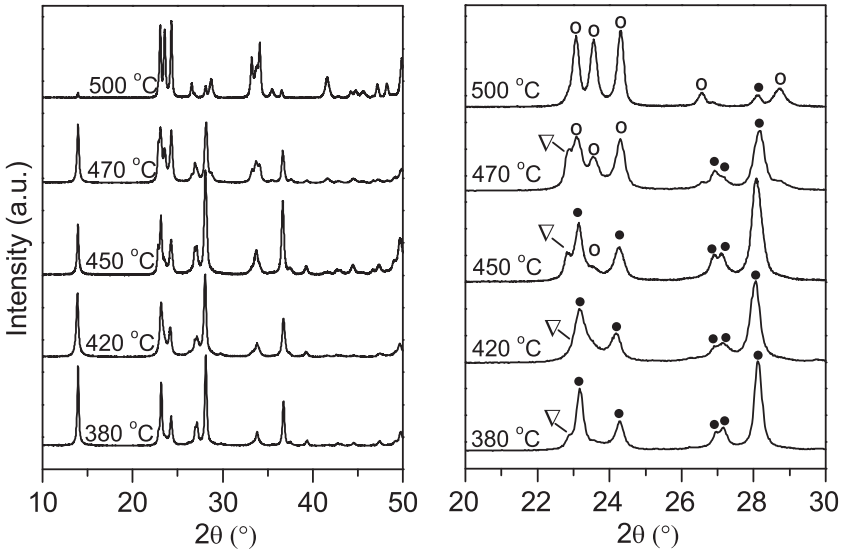

Fig. 2. XRD patterns of NbW_{60} prepared by precipitation and calcined at increasing temperatures: (○) m-WO_3, (●) h-WO_3 and (▽) H_xWO_{3-y} (the right panel shows a magnified region of the left spectra).

on these findings, it is reasonable to postulate that the HATB/h-WO_3 material formed at 380 °C in the present study is due to the transformation of the partly crystalline precursor formed upon solvent evaporation and heating in air to 380 °C. The observation that the amount of HATB decreases at intermediate temperatures may be explained by its transformation into h-WO_3 upon removal of ammonia. The hexagonal phases present in our samples are seen to evolve in a similar way as reported during AMT decomposition. A difference with the literature work on AMT decomposition is that small amounts of THTB were observed in the present work when the precursor was calcined in the temperature range of 370–450 °C. The fraction of THTB is greatest after calcination at 450 °C. The formation of THTB has also been reported by decompostion of ammonium paratungstate (APT) in H_2/He [29]. It was therein found that when APT is heated rapidly, more ammonium ions remain occluded in the crystalline phase, inducing formation of HATB. Comparatively, slow heating of APT led to predominantly THTB, attributed to more efficient removal of ammonia.

We also investigated the calcination of mixed oxides of Nb and W obtained from AMT and ammonium niobate oxalate hydrate, $NH_4NbO(C_2O_4)_2{\cdot}xH_2O$. The XRD patterns of NbW_{60} (W/Nb ratio = 60) calcined at temperatures in the 380–500 °C range are shown in Fig. 2. The structural transformations observed for NbW_{60}-*T* are similar to those for WO_3-*T*. The dominant phase after calcination at 420 °C is h-WO_3 with a very small amount of THTB. The THTB content increases when NbW_{60} is calcined at higher temperature. Almost no THTB is observed anymore in NbW_{60}-500. In contrast to WO_3-500, NbW_{60}-500 still contains a small amount of h-WO_3 next to the dominant m-WO_3 phase. The oxalate anions from the niobium precursor and, also, ammonia from the Nb and W precursors facilitate formation of h-WO_3 [11].

Table 1 also lists the textural properties of these oxides. Expectedly, the surface areas for WO_3-*T* are relatively small and decrease with increasing calcination temperature. There is no systematic trend with the Nb content for the NbW_x materials. The Nb/W ratios as measured by XPS (Table 1) are in reasonable agreement with the Nb/W ratios of the initial solutions. The morphology of a few samples was further analyzed by SEM. It shows that the materials calcined at 420 °C (WO_3 and NbW_{60}) consist of agglomerates of primary particles of about 50 nm. When calcined at 500 °C, the particle size is larger at about 100 nm, consistent with the decrease in surface area.

Table 2
TPR data for WO_3-*T* and Pd/WO_3-*T* materials.

Sample	First reduction feature		Total n_{H_2} (mmol/g)	H_2/WO_3
	n_{H_2} (mmol/g)	*T* (°C)		
WO_3-380	0.29	670	1.8	0.14
Pd/WO_3-380	0.37	435	2.9	0.22
WO_3-420	0.69	594	2.9	0.22
Pd/WO_3-420	0.47	435, 560	3.4	0.26
WO_3-450	0.51	584	3.2	0.24
Pd/WO_3-450	0.36	430, 560	3.2	0.24
WO_3-470	0.28	653	2.4	0.18
Pd/WO_3-470	0.23	435, 545	3.3	0.25
WO_3-500	0.21	650	1.8	0.14
Pd/WO_3-500	0.36	395	4.5	0.34

As will be shown below that calcination at intermediate temperatures yields the most acidic materials, we also varied the W/Nb ratio of the mixed oxides NbW_x and investigated such samples upon calcination at 420 °C and 450 °C. The XRD patterns and the contribution of the various identified phases are given in Fig. 3 and Table 1, respectively. Their structures resemble those of the mixed Nb_2O_5-WO_3 material (W/Nb = 10) prepared by Arata and co-workers by a similar co-precipitation method [15]. All NbW_x samples calcined at 420 °C contain h-WO_3. The broadening of the XRD reflection around 23.15° for NbW_{45}-420 and NbW_{120}-420 points to small amounts of THTB in the tungsten-rich formulations. When these samples were calcined at 450 °C, more ammonia was removed and the main phases present in the NbW_x-450 set were h-WO_3 and m-WO_3 with small amounts of THTB. With increasing W/Nb ratio the ammonia and water content was lower and, consequently, the NbW_{120}-450 mainly contains THTB and m-WO_3 (Fig. 4).

The weight-loss curves obtaining during TG analysis of the WO_3 precursor samples are collected in Fig. 5. The water and ammonia content derived from these curves are summarized in Table 1. For WO_3-380 the weight loss takes predominantly place between 350 and 550 °C, which can be related to the removal of ammonia and water in the structure [11]. The small weight loss at lower temperatures is due to removal of physisorbed water. The materials that were calcined at 420 and 450 °C contain more water, as evidenced by the more substantial weight loss below 300 °C. As shown in Table 2, the content of ammonia and structure water in WO_3-420 is very similar (ca. 0.5 wt%) with that of WO_3-380,

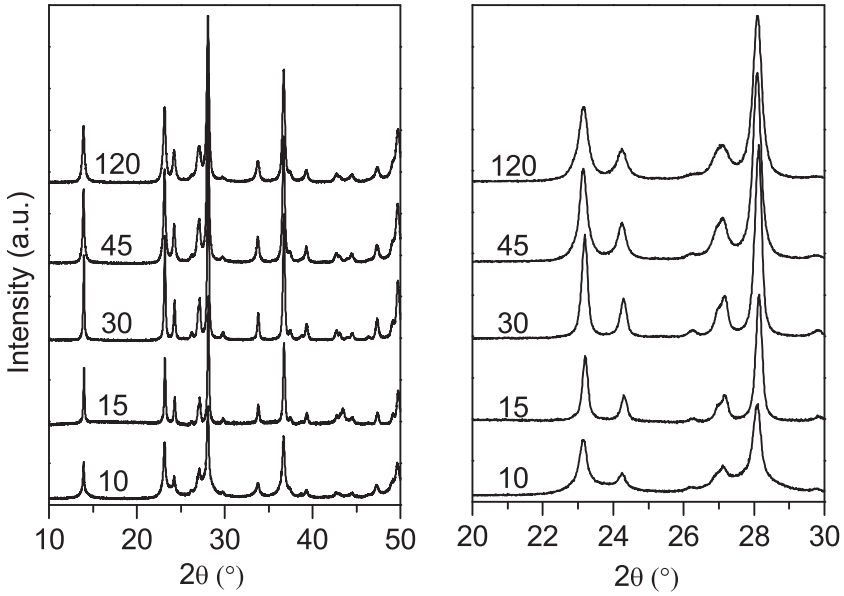

Fig. 3. XRD patterns of NbW_x-420 with different W/Nb ratios prepared by precipitation of a solution containing ammonium metatungstate and ammonium niobate oxalate hydrate followed by calcination at 420 °C (the right panel shows a magnified region of the left spectra).

whereas it is much lower for WO_3-450. Together with the XRD analysis, these data indicate that HATB obtained after 380 °C calcination has converted into h-WO_3, resulting in additional water absorption at ambient conditions. The TG curves of WO_3-470 and WO_3-500 contain evidence of further ammonia removal, consistent with the almost exclusive presence of m-WO_3. Thus, upon removal of ammonia the material restructures into the monoclinic form of WO_3. Qualitatively, these trends are similar for the NbW_x samples. Notably, the NbW_x-420 samples contain more ammonia and chemisorbed water than the WO_3 samples and also than the NbW_x-450 ones. The ammonia and chemisorbed water content is highest for NbW_{10}-420 (0.7%). Calcination at 450 °C resulted in much lower content of ammonia and chemisorbed water of the NbW_x materials, typically around 0.2%. Attempts to quantify the amount of nitrogen in these materials by XPS or EDX were not fruitful due to the small NH_3/NH_4^+ content.

Crystalline WO_3 is a semiconductor with a band gap of 2.85 eV. Weber established by optical spectroscopy that the lowest energy width of the band gap is proportional to the number of next-nearest W (Mo) neighbors for W—O (Mo—O) compounds [30,31]. The band gap can be determined from linear extrapolation to zero absorption in plots of $[F(R_\infty)h\nu]^2$ *vs.* $h\nu$, where $F(R)$ is the Kubelka–Munk function, h Plank's constant and ν the frequency [30]. As reference values, the band gaps of 2.85 eV for bulk WO_3 and 3.45 eV for $(NH_4)_6H_2W_{12}O_{40}$ with six and four next-nearest W neighbors, respectively, can be used. The band gap values for WO_3-*T* including a commercial WO_3 powder (m-WO_3 according to XRD) are collected in Table 1. Fig. S2 shows the corresponding plots. The band gap of WO_3-500 is similar to that of the commercial m-WO_3 reference. The values for WO_3-420 and WO_3-450 are 3.1 eV, while those of WO_3-380 and WO_3-470 containing a substantial fraction of m-WO_3 are 3.0 eV. In accordance with literature [31], we find that

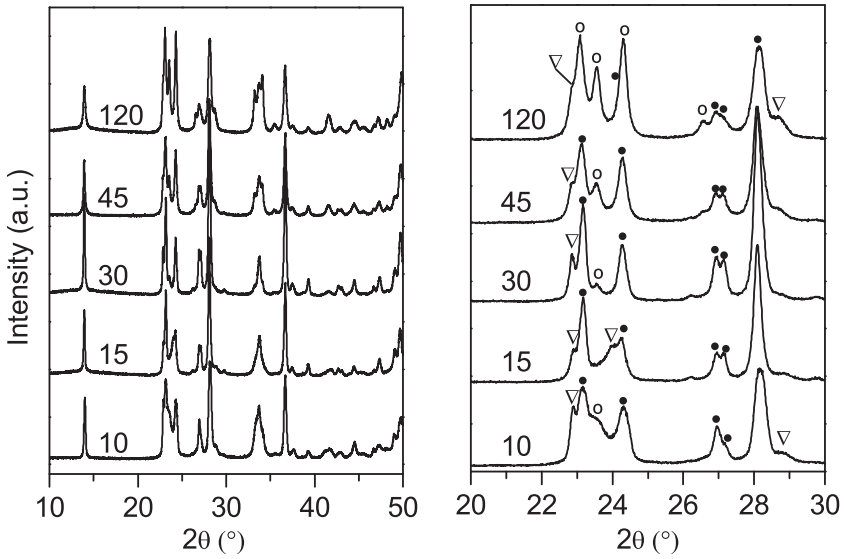

Fig. 4. XRD patterns of NbW_x-450 with different W/Nb ratios prepared by precipitation of a solution containing ammonium metatungstate and ammonium niobate oxalate hydrate followed by calcination at 450 °C (the right panel shows a magnified region of the left spectra): (○) m-WO_3, (●) h-WO_3 and (▽) H_xWO_{3-y} (THTB).

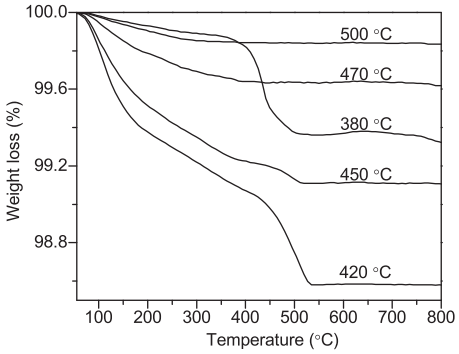

Fig. 5. TG curves of WO_3-*T* samples after varying calcination temperatures.

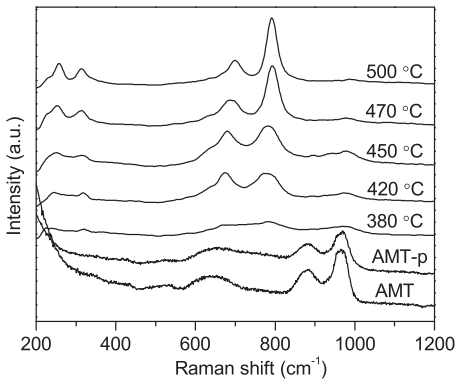

Fig. 6. UV-Raman spectra of AMT, AMT-p and the WO_3-*T* samples after increasing calcination temperature (excitation with 325 nm laser).

the average number of covalent bridging W—O—W of the central W cation is about six for WO_3-500, suggesting an infinite network of WO_6 octahedra, whereas it is around five for the hexagonal WO_3 phases in WO_3-420 and WO_3-450. The other two materials have intermediate next-nearest neighbor W numbers, consistent with the finding that they are mixtures of m-WO_3 and h-WO_3 phases. The band gap energies of NbW_x-420 samples are around 3.1–3.2 eV with NbW_{30}-420 as an outlier, whereas the higher content of m-WO_3 of the corresponding samples calcined at 450 °C is evident from the lower band gap energies. For completeness, we mention that the corresponding values for AMT and the commercial WO_3 sample are 3.46 eV and 2.76 eV respectively, indicative of polymeric WO_6 cluster in AMT and an infinite three-dimensional network of WO_6 units in the commercial m-WO_3 sample.

Raman spectra of the WO_3-*T* set are presented in Fig. 6. The spectrum of the AMT precursor contains signature bands of distorted WO_6 units. Clear Raman features are seen at 960 ($\nu_{s,W=O}$), 882 ($\nu_{as,W=O}$) and W—O—W modes at 640 cm^{-1}. The Raman features of the re-precipitated AMT precursor indicate that no substantial transformation has occurred. The broad Raman bands for WO_3-380 are consistent with the finding from XRD that the original structure of the AMT precursor has not been retained. The bands between 200 and 350 cm^{-1} are O—W—O deformation bands and the ones around 672 cm^{-1} and 780 cm^{-1} correspond to stretching modes of O—W—O [32]. Their presence indicates that part of the WO_6 octahedra in WO_3-380 are connected after partial removal of water and ammonia. The weak bands at 638, 687 and 781 cm^{-1} are assigned to HATB and/or h-WO_3 [29]. The more pronounced bands at 641, 672 and 780 cm^{-1} for WO_3-420 and NbW_x-420 (Fig. S3) should be related to h-WO_3 [29]. The latter band shifts to 792 cm^{-1} and becomes more intense for samples calcined at higher temperature. For the monoclinic samples obtained at high temperature, the stretching model of terminal W=O at 988 cm^{-1} is very weak, likely due to the large size of the m-WO_3 crystals.

TPR was used to study the reduction of the (mixed) oxide samples. The various steps involved in WO_3 reduction have been well documented in literature [33]. Fig. 7 shows the TPR traces for the WO_3-*T* materials. The quantitative results are collected in Table 2. The TPR traces show more than one reduction feature due to the mixture of tungsten oxide phases. This first reduction step started at lower temperature for WO_3-420 and 450 (590 °C) compared with the other samples (650–670 °C). Previously, it has been found that reduction of the WO_3 below 800 °C results in phases such as $WO_{2.9}$, $WO_{2.72}$ and $WO_{2.83}$ [13]. The total H_2 consumption (Table 2) suggests that such phases are formed, although the exact stoichiometry cannot be deduced. The total H_2 consumption below 800 °C is higher for WO_3-420 and -450 than for the other three samples. Together with the TG analysis showing that these two samples contain more water the deeper reduction of WO_3-420 and 450 is consistent with literature stating that more $WO_{2.72}$ is formed when the water content of the starting tungsten oxide phase is higher [34,35]. The TPR traces for NbW_x-420 and 450 are shown in Fig. 8a and b, respectively. The presence of ammonia in the structure of WO_3 influences the first reduction feature. The temperature of this reduction feature of NbW_x-450 is higher than that of WO_3-420, which points to stronger binding of WO_x with NbO_x in the former structure, consistent with the reported more difficult reduction of mixed oxides [14]. The temperature of the first reduction feature of the NbW_x set increases with decreasing W/Nb ratio (increasing Nb content) and we assume that it trends with the ammonia content.

As we will employ these oxide materials as the acidic component in bifunctional hydroconversion catalysts with Pd providing the metal (de)hydrogenation function, we also investigated Pd/WO_3 and Pd/NbW_x by TPR. These traces (Fig. 8c and d) are different from the ones for the parent oxides. Typically, the presence of Pd facilitates reduction processes due to spillover effects, as evident in the present materials from the lower reduction temperatures. All traces for Pd-containing samples in Fig. 8 contain a H_2 production feature at relatively low temperature, which is due to the release of H_2 from Pd-hydrides formed at lower temperatures. It shows that the Pd phase is well reduced. The first reduction peak for Pd/WO_3-*T* occurs between 420 and 560 °C, significantly lower than for the corresponding WO_3-*T* materials [36,37]. Pd/WO_3-420, which is mainly composed of h-WO_3, showed small and large first reduction peaks at 430 and 560 °C, respectively. The low-temperature feature is likely due to reduction of THTB and the other high-temperature feature is attributed to reduction of h-WO_3. Consistent with this, the higher amount of THTB in WO_3-450 resulted in greater H_2 consumption at 430 °C. The features for THTB and h-WO_3 are absent in WO_3-470 and WO_3-500, which mainly contain m-WO_3. The small feature around 400 °C observed for WO_3-500 is due to the reduction of m-WO_3 to the hydrogen tungsten bronze [13]. The first reduction feature of m-WO_3 occurs at lower temperature than that of h-WO_3. We speculate that ammonia located in the hexagonal channels of the h-WO_3 structure limits reduction of h-WO_3. Two different reduction features are observed in the H_2-TPR patterns of Pd/NbW_x-420, which mainly contains h-WO_3. The high-temperature feature between 560 and 610 °C is attributed to the reduction of h-WO_3. The low-temperature feature between 505 and 530 °C is attributed to the reduction of THTB in NbW_x-420, although it was very difficult to derive the presence of THTB from the XRD patterns in NbW_x-420 with $x = 10$, 15 and 30. The temperature of first reduction feature for Pd/NbW_x-420 increases with decreasing W/Nb ratio, which is caused by the strong bonding of WO_x with NbO_x. The first reduction process of Pd/NbW_x-450 containing a mixture of oxides is more complicated than that of Pd/NbW_x-420. Besides the temperature features for THTB reduction (505–535 °C) and h-WO_3 reduction (550–610 °C), there are

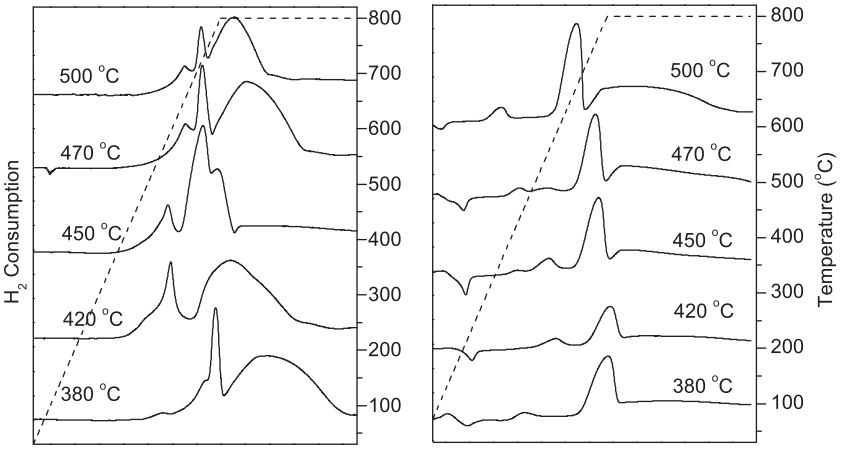

Fig. 7. TPR profiles for (left) WO_3 and (right) Pd/WO_3 prepared at increasing temperatures.

additional small reduction features around 430 °C, which should be due to the first reduction of m-WO_3.

XPS was used to investigate the W oxidation state in WO_3-*T*. The spectra are shown in Fig. 9. For the W $4f_{7/2}$ binding energies we used the following reference values [29,38,39]: W^{6+} at 35.2–35.7 eV, W^{5+} at 33.9–34.5 eV, W^{4+} at 33.1–33.5 eV, $W^{\delta+}$ at 31.5 ± 0.1 eV and W^0 at 30.9 ± 0.1 eV. The results of deconvolution of the W 4f XP spectra for WO_3-*T* are given in Table 3. Mixed oxidation states of tungsten were observed in WO_3-*T* series with a W^{5+}/W^{6+} ratio close to 0.1, which is similar to the XPS ratio for $WO_{2.96}$. [12,40]. The contribution of the W^{5+} component decreases with increasing calcination temperature, which can be related to the loss of ammonia. The W^{5+} component in WO_3-470 and 500 originates from the THTB intermediate. We also investigated the reduction of Pd/WO_3-*T* under conditions similar to those used in the pre-treatment of these materials as catalysts in alkane hydroconversion, namely reduction at 440 °C and 35 bar H_2. The corresponding spectra are given in Fig. 9 and the deconvolution results are listed in Table 3. The presence of W^{6+} and W^{5+} in the XP spectra of reduced Pd/WO_3-*T* is due to the presence of $(NH_4)_xWO_{3-z}$ or H_xWO_{3-z}. Elimination of hydrogen or ammonia from these structures results in WO_x sub-oxides with $x = 2.7–2.84$, which can be easily reduced to β-W. This reduced tungsten phase is observed in all of the reduced Pd/WO_3-*T* samples. Reduced Pd/m-WO_3 has been investigated before by XPS and XRD [13]. The results show that metallic tungsten is slowly formed during reduction. In De Angelis and Schiavello's report [40], the reduction degree of the WO_3 phase was estimated from the ratio of W^{5+}/W^{6+}. For instance, for the $WO_{2.72}$ sub-oxide the W^{6+} and W^{5+} contributions are estimated to be 44% and 56%, respectively. The W^{5+} content in reduced Pd/WO_3-*T* is significantly lower, which is evidence for the deeper reduction of W. No W^{5+} was observed anymore in reduced Pd/WO_3-500. Table 3 shows that Pd/WO_3-420 and -450 are not reduced as deeply as Pd/WO_3-380 and Pd/WO_3-500. Our explanation is that the ammonium bronze present on the surface of Pd/WO_3-420 and 450 limits the reduction. This speculation is supported by the TPR results that show that the surface of samples containing m-WO_3 is easier reduced than the surface of samples containing mainly h-WO_3. The W^0 content in reduced Pd/WO_3-380 is almost as high as in reduced Pd/WO_3-500, but in reduced Pd/WO_3-380 there is still W^{5+} present. This is likely due to the mixture of h-WO_3 and amorphous tungsten oxide phases in Pd/WO_3-380, limiting deep reduction to W^0.

The W oxidation state distribution is very similar for NbW_x-420 and NbW_x-450. The W^{5+} component in NbW_x-420 mostly originates from HATB, while in NbW_x-450 it stems also from THTB. The W^{6+} content in reduced Pd/NbW_x-420 is about 67% (Table 3), nearly similar to the value for Pd/NbW_x-420. A small amount of metallic W, typically about 3%, was formed in all reduced Pd/NbW_x-420

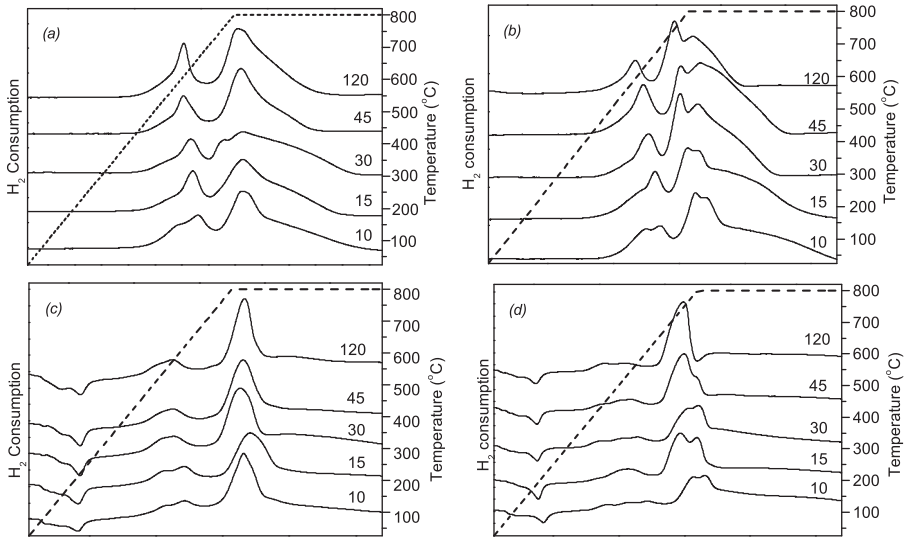

Fig. 8. TPR profiles for (a) NbW_x-420, (b) NbW_x-450, (c) Pd/NbW_x-420 and (d) NbW_x-450.

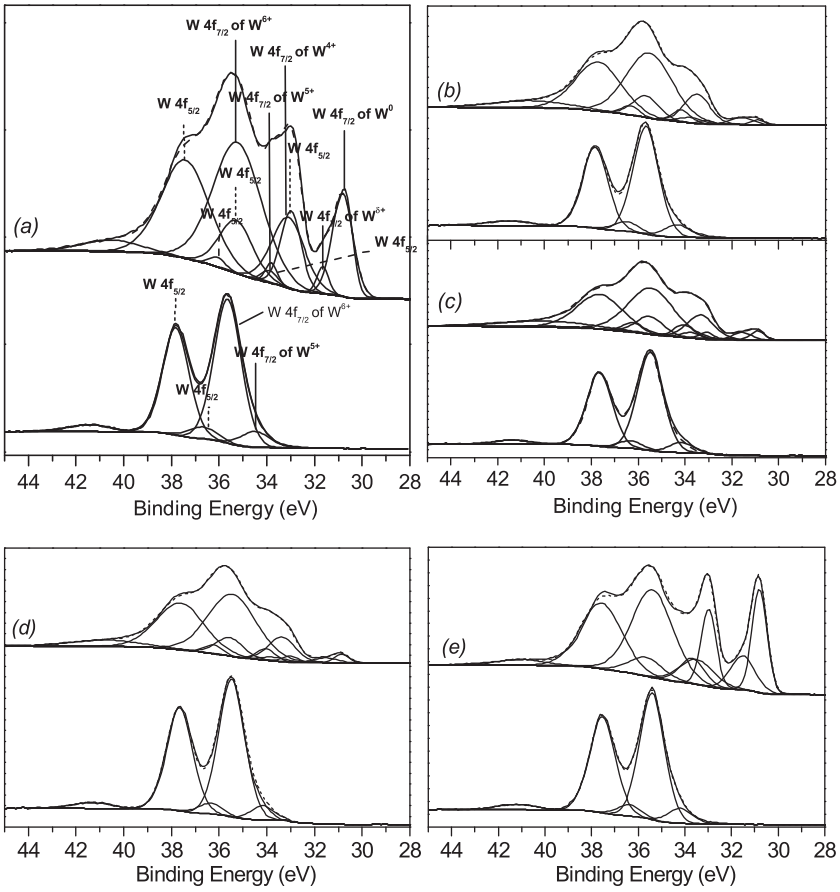

Fig. 9. XPS profiles of WO_3 and reduced Pd/WO_3 calcined at (a) 380 °C, (b) 420 °C, (c) 450 °C, (d) 470 °C, (e) 500 °C.

Table 3
W speciation in calcined WO_3-*T* and reduced Pd/WO_3-*T* (*T* = 440 °C and $P_{hydrogen}$ = 35 bar) as determined by W 4f XPS analysis.

Sample	W^{6+} (eV/%)	W^{5+} (eV/%)	W^{4+} (eV/%)	$W^{\delta+}$ (eV/%)[a]	W^0 (eV/%)
WO_3-380	35.7/86	34.5/14	–	–	–
Pd/WO_3-380	35.2/52	33.9/12	33.1/13	31.6/3	30.8/20
WO_3-420	35.7/88	34.3/12	–	–	–
Pd/WO_3-420	35.7/68	34.2/6	33.5/20	31.6/4	30.9/2
WO_3-450	35.5/91	34.2/9	–	–	–
Pd/WO_3-450	35.5/60	34.1/11	33.3/21	31.6/4	30.9/4
WO_3-470	35.6/90	34.2/9	–	–	–
Pd/WO_3-470	35.6/65	34.0/9	33.4/19	31.5/2	30.8/5
WO_3-500	35.4/92	34.3/8	–	–	–
Pd/WO_3-500	35.4/46	0	33.5/18	31.5/12	30.8/24

[a] Intermediate tungsten state between W^{4+} and W^0 [38].

samples. Also, more metallic W is present in reduced Pd/NbW_x-450, consistent with the increasing contribution of the THTB component in the parent NbW_x-450 sample. The W^{6+} composition in reduced Pd/NbW_x-450 is similar as in the reduced Pd/NbW_x-420, indicating almost similar reduction degree for Pd/NbW_x-420 and 450 at 35 bar and 440 °C.

The XRD patterns of reduced Pd/WO_3-*T* are shown in Fig. 10. Consistent with the XPS results, β-W was observed in several samples and its contribution was highest in reduced Pd/WO_3-380 and Pd/WO_3-500. The XRD pattern of reduced Pd/WO_3-380 also shows the presence of HATB, which derived from reduction of h-WO_3. No β-W was observed in reduced Pd/WO_3-420, in line with the difficulty to reduce this sample. From XRD it follows that HATB is the main phase. Fig. 11 shows the corresponding XRD patterns of the Pd/NbW_x-420 and Pd/NbW_x-450 sets of samples. Similar to Pd/WO_3-420, HATB is the main phase in reduced Pd/NbW_x-420.

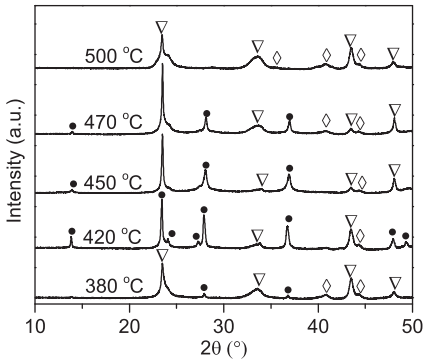

Fig. 10. XRD patterns for reduced Pd/WO_3 prepared at different temperatures: (▽) THTB, (●) HATB, (◊) β-W.

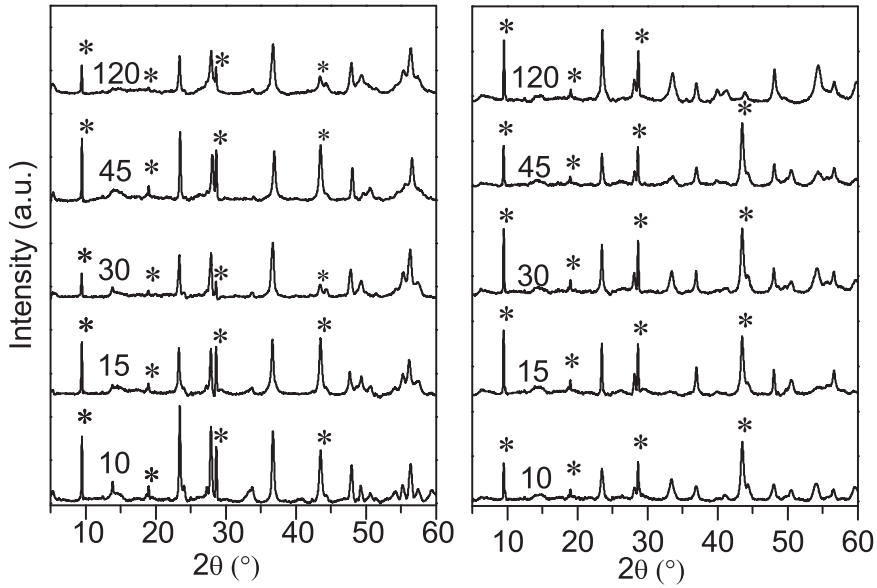

Fig. 11. XRD patterns for reduced of Pd/NbW_x prepared at (left) 420 °C and (right) 450 °C at different W/Nb ratios (* are reflection of the Kapton foil to protect sample against air oxidation).

Reduced Pd/NbW_{10}-420 mainly contains HATB, in agreement with TG and XPS results. Due to the decreasing ammonia content in NbW_x-450, the phase formed during reduction of Pd/NbW_x-450 is nearly similar to that in reduced Pd/NbW_x-420. The resulting phase has the overall formula $(NH_4)_{0.33-x}(H_3O)_yWO_{3-z}$. The partial removal of ammonia is speculated to give rise to Brønsted acidity. It appears that the main difference between $(NH_4)_{0.33-x}(H_3O)_yWO_{3-z}$ and HATB is the lower ammonia content in the former.

On the basis of the above findings, the properties of WO_3 are summarized schematically in Fig. 12. The structure of WO_3 is influenced by the calcination temperature and the ammonia content. The first reduction step for WO_3 samples containing predominantly h-WO_3 occurred at lower temperature than WO_3 containing more m-WO_3. This order reverses when Pd metal is present during the reduction process. $(NH_4)_{0.33-x}(H_3O)_yWO_{3-z}$ is present in reduced Pd/h-WO_3, while the main phases are H_xWO_{3-z} and β-W in reduced Pd/m-WO_3.

Acid-catalyzed hydroisomerization of *n*-heptane was used to evaluate the acidity of Pd/WO_3-*T* samples. The Pd metal catalyzes the dehydrogenation of alkanes to intermediate olefins, which are isomerized and/or cracked on the Brønsted acid sites [24,41,42]. The amount of Pd is chosen such that the hydrogenation/dehydrogenation reactions of alkanes/alkenes are equilibrated [42]. Under such conditions, the reaction rate is controlled by the acid-catalyzed conversion of the intermediate olefins. The temperature to achieve an *n*-heptane conversion of 40% is used as the activity parameter. Careful inspection of literature shows that unsupported WO_3 and their Nb-promoted analogues have earlier been evaluated in several acid-catalyzed reactions [12,23,24], yet a thorough comparison in a hydrocarbon conversion reaction requiring strong Brønsted acidity has not been undertaken yet. Hydroisomerization of *n*-paraffins is important for the manufacture of high-octane blending components and lubricants. The results for *n*-heptane hydroconversion results for the Pd/WO_3-*T* and Pd/NbW_x sets are listed in Tables 4 and 5. To facilitate comparison, we use WO_3-380 as the reference acid catalyst. The parameter k/k_{ref} is the relative activity of a particular material to this reference catalyst. We also report the apparent activity energies. Pd/WO_3-420 and Pd/WO_3-450 are the most acidic materials in the Pd/WO_3-*T* set.

Table 4
Catalytic activities of reduced Pd/WO_3-*T* in the hydroconversion of *n*-heptane ($P_{hydrogen}$ = 35 bar; H_2/alkane ratio = 24).

Catalyst		SA[a] (m^2/g)	T_{40} (°C)	E_{act} (KJ/mol)	k/k_{ref}
Pd/WO_3-*T*	380	12	313	139	1.0
	420	4	272	124	6.8
	450	7	271	123	7.0
	470	7	283	123	3.7
	500	6	299	152	2.1
	800	1	330	126	0.5
Pd/WZr(4.5)		26	353	192	0.1
Pd/WZr(13.5)		45	300	155	2.0
Pd/WZr(18)		26	334	177	0.3
ASA(co-gel)[b]		463	326	120	0.6
USY[c]		-	233	128	64
H-ZSM-5[c]		371	221	159	436
Al-SBA-15[d]		842	307	135	1.3

[a] BET surface area.
[b] Amorphous silica-aluminas prepared by cogelation with SAR = 19 from Ref. [37].
[c] Ultrastabilized Y (USY) with SAR = 8 and H-ZSM-5 with SAR = 40.
[d] Aluminum-containing SBA-15 taken from Koekkoek et al. [38].

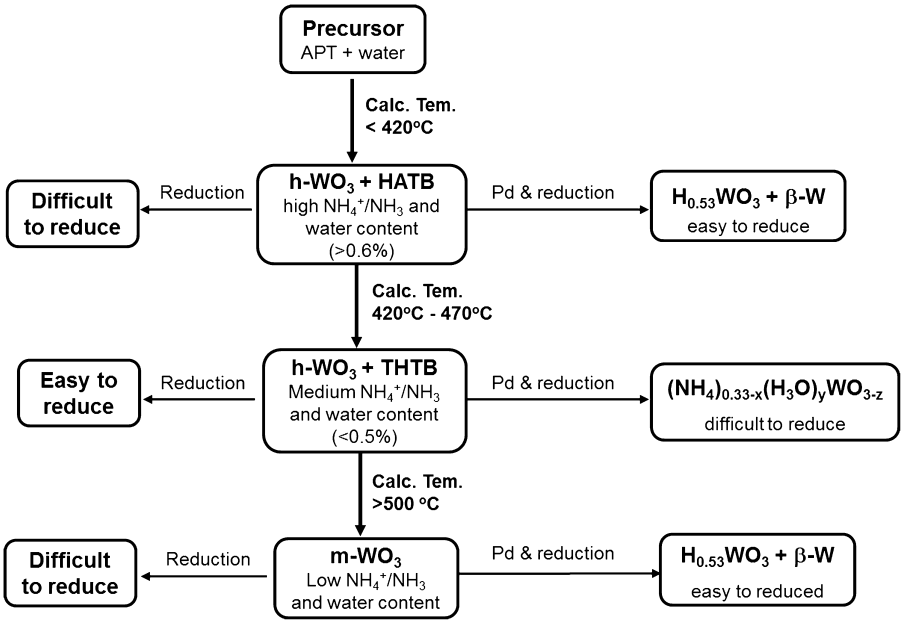

Fig. 12. Scheme for the WO_3 phase transformation and surface reduction.

Table 5
Catalytic activities of reduced Pd/NbW_x-420 and -450 in the hydroconversion of *n*-heptane ($P_{hydrogen}$ = 35 bar; H_2/alkane ratio = 24).

Catalyst		T_{40} (°C)	E_{act} (kJ/mol)	k/k_{ref}
Pd/WO_3-380		313	139	1.0
Pd/NbW_x-420	10	313	148	1.0
	15	329	135	0.5
	30	299	137	2.0
	45	321	143	0.7
	120	295	136	2.4
Pd/NbW_x-450	10	280	120	4.3
	15	283	125	4.0
	30	275	116	5.2
	45	270	119	6.9
	120	267	114	7.3

Pd/WO_3-800 (WO_3 calcined at 800 °C, not further characterized) displayed much lower activity. Table 4 also contains kinetic data for a number of other tungsten-oxide catalysts and aluminosilicate acidic catalysts. WO_x/ZrO_2 catalysts have been described as strongly acidic components in hydrocarbon conversion catalysts [24,43]. Three zirconia-supported WO_3 catalysts were prepared following established procedures at WO_3 loadings of 4.5, 13 and 18 wt% [24]. Pd-loaded WZr(13.5) was the most active isomerization catalyst in this set. Its acidity is close to that of Pd/WO_3-500, but substantially lower than the optimum Pd/WO_3-*T* catalysts. The finding that the acidity is highest at intermediate WO_3 loading is consistent with literature [24]. This optimum has been related to WO_x clusters with intermediate surface density for high densities of Brønsted acid sites [9,24] and is argued to be related to a balance between reducibility and accessibility. Very small clusters of WO_x cannot be reduced, whereas accessibility of the acid sites formed in large clusters is limited. These reports also emphasize that the presence of Pd facilitates the formation of Brønsted acid sites by spillover of H atoms to partially reduce the WO_x surface. Also amorphous aluminosilicates including Al-SBA-15 were less acidic than the Pd/WO_3 materials. On the contrary, an ultrastabilized Y (steam-calcined faujasite) and H-ZSM-5 zeolites display substantially higher acidity than the WO_3-*T* materials. Table 5 reports the activities of Pd-containing mixed oxides Pd/NbW_x-450 with W/Nb ratios of 45 and 120. The starting materials contain mixed m-WO_3/h-WO_3 phases at low ammonium content in which part of W has been substituted by Nb. These materials show similar catalytic activities as optimum Pd/WO_3 catalysts. When the W/Nb ratio of Pd/NbW_x-450 is below 30 the catalytic activity is much lower. The H_2-TPR analysis shows that these oxides are more difficult to reduce, which is attributed to a greater proportion of Nb—O—W bonds for samples with lower W/Nb ratio. This lower reducibility lowers the number of acid sites. The Pd/NbW_x-420 catalysts display lower activity than the Pd/NbW_x-450 ones at relatively high Nb content. Besides the influence of Nb, the lower calcination temperature left more ammonium in the structure of the Pd/NbW_x-420 materials, which also causes lower acidity.

Interestingly, WO_3 obtained by a simple procedure and with a relatively low surface area renders excellent acid catalysts. The Brønsted acidity is intermediate to the acidities of amorphous silica–aluminas and crystalline zeolites, two important classes of industrial acidic materials. The tungsten oxide materials are also more acidic than zirconia-supported WO_3, which has been extensively investigated as promising alternative acids in the last decade. An important aspect in *n*-alkane hydroisomerization is to avoid as much as possible cracking reactions, which would result in undesired gas make. To compare the various catalysts in this regard, Fig. 13 shows the C_7-isomer selectivity as a function of *n*-heptane conversion. Data are reported for *n*-heptane conversion levels below 50%. The most acidic materials, Pd/WO_3-420 and Pd/WO_3-450, show excellent isomerization selectivity in excess of 90% at all conversion levels. The selectivity for Pd/WZr(13.5) as a function of conversion is very similar. The Pd/WO_3-*T* materials calcined at 380, 470 and 500 °C show lower isomerization selectivities, albeit that the performance of these materials is still better than that of Pd/HZSM-5. Notably, the suboptimal Pd/WZr(4.5) and Pd/WZr(18) catalysts have low isomerization selectivities. Thus, we conclude that optimum Pd/WO_3 catalysts are much more active than optimum Pd/WO_x/ZrO_2 catalysts in the hydroisomerization of *n*-heptane at similar isomerization yield. The isomerization selectivity for Pd/NbW_x-450 is similar to those for Pd/WO_3-420 and Pd/WO_3-450, which suggests that the Brønsted acid sites in Pd/NbW_x-450 are of similar strength to those in Pd/WO_3-420 and 450. Although the isomerization selectivity for Pd/NbW_x-420 with

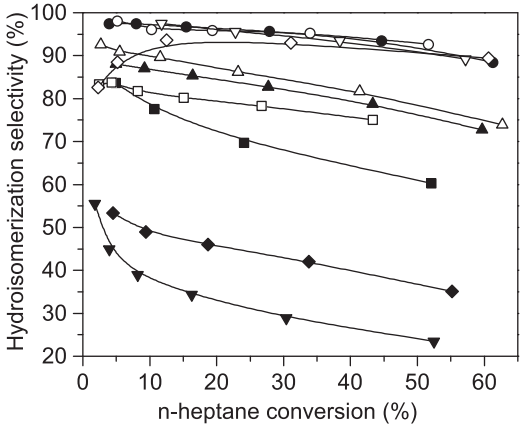

Fig. 13. Hydroisomerization of *n*-heptane: (□) Pd/WO_3-380, (●) Pd/WO_3-420, (○) Pd/WO_3-450, (▲) Pd/WO_3-470, (△) Pd/WO_3-500, (▼) Pd/4.5WZr, (▽) Pd/13.5WZr, (♦) Pd/18WZr, (■) HZSM-5 and (◊) HZSM-5 nanosheets.

x = 10, 30 and 120 is also as high as 90% for the most active catalysts, other samples in the Pd/NbW_x-420 set exhibit lower isomerization selectivities.

For WO_3/ZrO_2 acidic materials the Brønsted acid sites are argued to derive from a partially reduced surface oxide phase in which the negative charge delocalized across the W—O—W network is neutralized by a proton [44,45]. The formation of Brønsted acid sites during reduction in hydrogen has been directly observed by pyridine IR measurements for Pt/WO_3-ZrO_2 by Hattori et al. [46]. It was found that Lewis acid sites were converted to Brønsted acid sites during reduction. Formation of Brønsted acid sites in this way also closely resembles strong acidity development in heteropolytungstate clusters [47]. In 12-tungstophosphoric acid, the neutral $(WO_3)_{12}$ shell around the central $(PO_4)^{3-}$ anion delocalizes the negative charge over the surface of the shell, which is balanced by three acid hydrogens with a net positive charge to maintain electroneutrality of the cluster. In the present work, we also observe the formation of partially reduced WO_3 phases for reduced Pd/WO_3-*T*. IR measurements of adsorbed pyridine on these samples were unsuccessful because the samples are black after the reduction step.

Another aspect of the acidity is the ammonium content of the tungsten oxide phases. Pd/NbW_x-420 exhibits lower activity than Pd/NbW_x-450, although HATB is the main phase in both samples as follows from Fig. 12. The difference relates most likely to the lower ammonium content of NbW_x-450, which may imply that part of the ammonium ions have decomposed and the HATB phase has a higher proton density in the form of $(NH_4)_{0.33-x}(H_3O)_yWO_{3-z}$. The ammonia content of this phase is high enough to maintain the HATB structure in reduced Pd/NbW_x-450. The highest activity in the reduced Pd/NbW_x-450 was for x = 120, consistent with the lowest amount of ammonia left in this material. When ammonia is completely removed, a H_xWO_{3-z} bronze was formed in reduced Pd/WO_3-500. After calcination at 500 °C all ammonia has been removed and the acid activity is low. Comparing the various samples in terms of acidity and ammonia content, the acidity of $(NH_4)_{0.33-x}(H_3O)_yWO_{3-z}$ is stronger than that of H_xWO_{3-z}. It is instructive to compare this difference to the effect of alkali content on the acidity of heteropolyacid salts [47,48]. Heteropolyacid salts can be produced by partial proton exchange with alkali or other cations. For example, acidic $Cs_{2.5}H_{0.5}PW_{12}O_{40}$ can be obtained by partial exchange of the protons in the $H_3PW_{12}O_{40}$ with Cs^+. These acidic salts are water-insoluble and have higher surface area than the parent acid. Such partially exchanged heteropolyacid salts show higher catalytic activity for alkylation of m-xylene and 1, 3, 5-trimethylbenzene with cyclohexene [47] and have stronger acid sites than $H_3PW_{12}O_{40}$ [48]. It is likely that the proton density affects the strength of the acid sites and that this also plays a role in the $(NH_4)_{0.33-x}(H_3O)_yWO_{3-z}$ phases as investigated in the present work.

4. Conclusions

The transformation of re-precipitated $(NH_4)_6[H_2W_{12}O_{40}]\cdot 4H_2O$ and its mixture with $NH_4NbO(C_2O_4)_2\cdot xH_2O$ upon calcination was investigated. Calcination of the initial disordered $WO_3\cdot nH_2O$ phase resulted in a mixture of HATB and h-WO_3 at low temperature and in m-WO_3 at high temperature. h-WO_3-type phases were found to be dominant at intermediate calcination temperature. The hexagonal phase is stabilized by NH_3 and NH_4^+. Temperature-programmed reduction measurements show that the reducibility depends strongly on the initial tungsten oxide phase obtained after calcination. The presence of Pd increases the reducibility. Samples containing m-WO_3 were easily reduced with β-W as the main product. We found that $(NH_4)_{0.33-x}(H_3O)_yWO_{3-z}$ was formed when h-WO_3 phases obtained at intermediate calcination temperatures were reduced in the presence of Pd. High catalytic activity in the hydroconversion of *n*-heptane with very high isomer selectivity is associated with the presence of this bronze phase. Thus prepared tungsten and mixed niobium oxide are highly acidic catalysts, more acidic than amorphous silica-alumina and tungstated zirconia, as validated by *n*-heptane hydroisomerization.

Acknowledgments

The authors thank Shell Global Solutions for financial support.

Appendix A. Supplementary data

Supplementary data associated with this article can be found, in the online version, at http://dx.doi.org/10.1016/j.apcatb.2014.08.008.

References

[1] M.M. Natile, F. Tomaello, A. Glisenti, Chem. Mater. 18 (2006) 3270.
[2] T. Onfroy, G. Clet, M. Houalla, J. Phys. Chem. B 109 (2005) 3345.
[3] C. Matin, G. Solana, P. Malet, V. Rives, Catal. Today 2844 (2002) 1.
[4] M. Hino, K. Arata, J. Chem. Soc. Chem. Commun. (1988) 1259.
[5] K. Arata, M. Hino, Appl. Catal. A: Gen. 169 (1988) 151.
[6] J.G. Santiesteban, J.C. Vartuli, S. Han, R.D. Bastian, C.D. Chang, J. Catal. 168 (1997) 431.
[7] E. Iglesia, J.E. Baumgartner, F.H. Ribeiro, M. Boudart, J. Catal. 131 (1991) 523.
[8] R.A. Boyse, E.I. Ko, J. Catal. 171 (1997) 191.
[9] W. Zhou, E.I. Ross-Medgaarden, W.V. Knowles, M.S. Wong, I.E. Wachs, C.J. Kiely, Nat. Chem. 1 (2009) 722.
[10] L.F. Chen, S.P. Ramirez Sebastian, J.A. Wang, Nanotechnology 1 (2013) 479.
[11] I.M. Szilagyi, J. Madarasz, G. Polol, P. Kiraly, G. Tarkanyi, S. Saukko, J. Mizsei, A.L. Toth, A. Szabo, K. Varga-Josepovits, Chem. Mater. 20 (2008) 4116.
[12] C. Bigey, G. Maire, J. Catal. 196 (2000) 224.
[13] C. Bigey, L. Hilaire, G. Maire, J. Catal. 184 (1999) 406.
[14] T. Shishido, H. Hattori, Appl. Catal. A: Gen. 146 (1996) 157.
[15] M. Hino, M. Kurashige, H. Matsuhashi, K. Arata, Appl. Catal. A: Gen. 310 (2006) 190.
[16] C. Tagusagawa, A. Takagaki, S. Hayashi, K. Domen, J. Phys. Chem. C 113 (2009) 7831.
[17] C.D. Baertsch, S.L. Soled, E. Iglesia, J. Phys. Chem. B 105 (2001) 1320.
[18] C.D. Baertsch, K.T. Komala, Y.H. Chua, E. Iglesia, J. Catal. 205 (2002) 44.
[19] T. Kim, A. Burrows, C.J. Kiely, I.E. Wachs, J. Catal. 246 (2007) 370.
[20] E.I. Ross-Medgaarden, W.V. Knowles, T. Kim, M.S. Wong, W. Zhou, C.J. Kiely, I.E. Wachs, J. Catal. 256 (2008) 108.
[21] M. Scheithauer, T.K. Cheung, R.E. Jentoft, R.K. Grasselli, B.C. Gates, H. Knozinger, J. Catal. 180 (1998) 1.
[22] R. Zhang, J.A. Schwarz, A. Datye, J.P. Baltrus, J. Catal. 138 (1992) 55.
[23] S.D. Jackson, B.J. Brandreht, D. Winstanley, Appl. Catal. 27 (1986) 325.
[24] D.G. Barton, S.L. Soled, G.D. Meitzner, G.A. Fuentes, E. Iglesia, J. Catal. 181 (1999) 57.
[25] J.B. Christian, M.S. Whittingham, J. Solid State Chem. 181 (2008) 1782.
[26] M.J.G. Fait, H.J. Lunk, M. Feist, M. Schneider, J.N. Dann, T.A. Frisk, Thermochim. Acta 469 (2008) 12.
[27] D. Hunyadi, I. Sajo, I.M. Szilagyi, J. Therm. Anal. Calorim. (2013), in press.

[28] I.M. Szilagyi, I. Sajo, P. Kiraly, G. Tarkanyi, A.L. Toth, A. Szabo, K. Varga-Josepovites, J. Madarasz, G. Pokol, J. Therm. Anal. Calorim. 98 (2009) 707.
[29] I.M. Szilagyi, F. Hange, J. Madarasz, G. Pokol, Eur. J. Inorg. Chem. (2006) 3413.
[30] R.S. Weber, J. Catal. 151 (1995) 470.
[31] M. Scheithauer, R.K. Grasselli, H. Knozinger, Langmuir 14 (1998) 3019.
[32] J. Nagai, Electrochim. Acta 46 (2001) 2049.
[33] W.D. Schubert, J. Ref. Hard Met. 9 (1990) 178.
[34] Z. Zou, J. Ref, Hard Met. 7 (1990) 57.
[35] D.C. Vermaire, P.C. van Berge, J. Catal. 116 (1989) 309.
[36] P. Arnoldy, J.C.M. De Jong, J.A. Moulijn, J. Phys. Chem. 89 (1985) 4517.
[37] G.C. Bond, J.B.P. Tripathi, J. Chem. Soc. Faraday Trans. 72 (1970) 933.
[38] F.Y. Xie, L. Gong, X. Liu, Y.T. Tao, W.H. Zhang, S.H. Chen, H. Meng, J. Chen, J. Electron Spectrosc. Relat. Phenom. 185 (2012) 112.
[39] J.R. Regalbuto, T.H. Flelsch, E.E. Wolft, J. Catal. 107 (1987) 114.
[40] R. Gehlig, E. Salje, A.F. Carley, M.W. Roberts, J. Solid State Chem. 49 (1983) 318.
[41] E.J.M. Hensen, D.G. Poduval, D.A.J.M. Ligthart, J.A.R. Van Veen, M.S. Rigutto, J. Catal. 269 (2010) 201.
[42] A.J. Koekkoek, J.A.R. van Veen, P.B. Gerrtisen, P. Giltay, P.C.M.M. Magusin, E.J.M. Hensen, Microporous Mesoporous Mater. 151 (2012) 34.
[43] M. Misono, Mater. Chem. Phys. 17 (1987) 103.
[44] A.M. Garrido Pedrosa, M.J.B. Souza, B.A. Marinkovic, D.M.A. Melo, A.S. Araujo, Appl. Catal. A: Gen. 342 (2008) 56.
[45] E. Iglesia, D.G. Barton, J.A. Biscardi, M.J.L. Gines, S.L. Soled, Catal. Today 38 (1997) 339.
[46] S. Triwahyono, T. Yamada, H. Hattori, Appl. Catal. A: Gen. 242 (2003) 101.
[47] J.B. Moffat, Stud. Surf. Sci. Catal. 20 (1985) 157.
[48] S. Soled, S. Miseo, G. McVicker, W.E. Gates, A. Gutierrez, J. Paes, Catal. Today 36 (1997) 441.